Two-fluid Numerical Simulations of the Origin of the Fast Solar Wind

D. Wójcik[1] , B. Kuźma[1], K. Murawski[1], and A. K. Srivastava[2]
[1] Group of Astrophysics, Institute of Physics, University of M. Curie-Skłodowska, ul. Radziszewskiego 10, 20-031 Lublin, Poland; dwojcik@kft.umcs.lublin.pl
[2] Department of Physics, Indian Institute of Technology (Banaras Hindu University), Varanasi-221005, India

Abstract

With the use of our JOANNA code, which solves radiative equations for ion + electron and neutral fluids, we perform realistic 2.5D numerical simulations of plasma outflows associated with the solar granulation. These outflows exhibit physical quantities that are consistent, to the order of magnitude, with the observational findings for mass and energy losses in the upper chromosphere, transition region, and inner corona, and they may originate the fast solar wind.

Key words: magnetohydrodynamics (MHD) – methods: numerical – solar wind – Sun: activity – Sun: corona

1. Introduction

The solar wind is a stream of energized, charged particles (primarily electrons and protons from hydrogen, along with atomic nuclei like helium, alpha particles) flowing outward from the Sun (Bierman 1951; Parker 1965). There is a fast, widely uniform wind, emanating from polar coronal holes and at a distance of 1 au from the Sun traveling at about $750 \, \mathrm{km \, s^{-1}}$, and a slow, sporadic one, pouring from active equatorial regions and moving at about half that speed. The magnetic field lines stretch out radially in coronal holes, and do not loop directly back to the Sun, providing an open path for the fast plasma to escape the grasp of gravity. As the corona expands, these winds must be replaced by plasma moving up from below to feed them.

In the modern era of high-resolution spaceborne and ground-based observations, special attention has been paid to studying the origin of plasma outflows that form the solar wind. Early models of the wind assumed the inner corona to be its origin (e.g., Tu 1987). Recently, Tu (2005) detected such outflows in coronal funnels at altitudes between 5 and 20 Mm above the photosphere, and found that they reach a speed of up to $10 \, \mathrm{km \, s^{-1}}$ at the height of 20 Mm. Emphasis was also placed on searching for the outflows in the chromosphere/transition region (e.g., Marsch et al. 2008; Tian et al. 2009; 2010; McIntosh et al. 2011; McIntosh 2012; Yang et al. 2013; Kayshap et al. 2015). It was found that these outflows can be generated by a variety of jets (De Pontieu et al. 2007; Wedemeyer-Böhm et al. 2012; Kayshap et al. 2013; Tian et al. 2014; Martínez-Sykora et al. 2017), and the injection of an often twisted magnetic field and its subsequent reconnection may also contribute to the bulk plasma outflows in coronal holes (e.g., Krieger et al. 1973; Zirker 1977; Kayshap et al. 2013; Yang et al. 2013).

It was showed theoretically that magnetohydrodynamic waves may be responsible for providing momentum to the upwardly moving plasma (e.g., Ofman 2005; Suzuki & Inutsuka 2005; Marsch 2006; Srivastava & Dwivedi 2006; De Pontieu et al. 2007; Arber et al. 2016). Among others, Hollweg (1978; 1981; 1986; Hollweg et al. 1982), Kudoh & Shibata (1999), and Matsumoto & Suzuki (2012) concluded that Alfvén waves possess a potential to drive plasma outflows. He et al. (2008) developed a model of plasma outflows in the coronal funnels, which includes Alfvén waves

(Ofman et al. 1995). Along this line of investigation, Yang et al. (2016) found that Alfvén waves are able to form fast plasma outflows. See also Ofman et al. (1995) and Shestov et al. (2017) for a similar analysis. However, Alfvén waves are difficult for detection, particularly when high-frequency waves are concerned (Srivastava et al. 2017); in an inhomogeneous and structured medium, these waves can experience reflection, mode coupling, phase-mixing, and resonant absorption (Ofman et al. 1995; Nakariakov et al. 1997; Zaqarashvili & Roberts 2006; Goossens et al. 2012; Chmielewski et al. 2014; Shestov et al. 2017).

Despite the abovementioned achievements, the origin of the solar wind still remains one of the central issues of heliophysics. We investigate here the role of granulation in generation of chromospheric ejecta and associated plasma outflows in coronal holes. We are motivated by the fact that a base of the corona is filled with dynamic jets, propelled from below the transition region upwards at speeds of about $25 \, \mathrm{km \, s^{-1}}$ into higher layers, that carry a significant amount of momentum (e.g., Sterling 2000; Zaqarashvili & Erdélyi 2009).

This paper is organized as follows. A physical model is presented in Section 2 and the corresponding numerical results are shown in Section 3. Our paper is concluded by discussion and summary of the numerical results in Section 4.

2. Two-fluid Model of a Partially Ionized Coronal Hole

We consider a solar coronal hole that is magnetically structured and gravitationally stratified, and its dynamics is described by two-fluid equations for ions + electrons treated as one fluid and neutrals regarded as second fluid. These equations can be written as follows:

$$\frac{\partial \varrho_n}{\partial t} + \nabla \cdot (\varrho_n \boldsymbol{V}_n) = 0, \tag{1}$$

$$\frac{\partial \varrho_i}{\partial t} + \nabla \cdot (\varrho_i \boldsymbol{V}_i) = 0, \tag{2}$$

$$\frac{\partial (\varrho_n \boldsymbol{V}_n)}{\partial t} + \nabla \cdot (\varrho_n \boldsymbol{V}_n \boldsymbol{V}_n + p_n \boldsymbol{I})$$
$$= \alpha_c (\boldsymbol{V}_i - \boldsymbol{V}_n) + \varrho_n \boldsymbol{g}, \tag{3}$$

$$\frac{\partial(\varrho_i V_i)}{\partial t} + \nabla \cdot (\varrho_i V_i V_i + p_{ie}I)$$
$$= \frac{1}{\mu}(\nabla \times B) \times B + \alpha_c(V_n - V_i) + \varrho_i g, \qquad (4)$$

$$\frac{\partial B}{\partial t} = \nabla \times (V_i \times B), \nabla \cdot B = 0, \qquad (5)$$

$$\frac{\partial E_n}{\partial t} + \nabla \cdot [(E_n + p_n)V_n] = \alpha_c V_n \cdot (V_i - V_n)$$
$$+ Q_n^{in} + q_n + \varrho_n g \cdot V_n, \qquad (6)$$

$$\frac{\partial E_i}{\partial t} + \nabla \cdot \left[\left(E_i + p_{ie} + \frac{B^2}{2\mu} \right) V_i - \frac{B}{\mu}(V \cdot B) \right]$$
$$= \alpha_c V_i \cdot (V_n - V_i) + Q_i^{in} + Q_R^i + q_i + \varrho_i g \cdot V_i, \qquad (7)$$

where the heat production terms are

$$Q_n^{in} = \alpha_c(\Delta\tilde{V} + \Delta\tilde{T}), \qquad (8)$$
$$Q_i^{in} = \alpha_c(\Delta\tilde{V} - \Delta\tilde{T}) \qquad (9)$$

with

$$\Delta\tilde{V} = \frac{1}{2}|V_i - V_n|^2, \qquad (10)$$

$$\Delta\tilde{T} = \frac{3k_B}{m_H(\mu_i + \mu_n)}(T_i - T_n), \qquad (11)$$

and the energy densities are given by

$$E_n = \frac{p_n}{\gamma - 1} + \frac{\varrho_n V_n^2}{2}, \qquad (12)$$

$$E_i = \frac{p_{ie}}{\gamma - 1} + \frac{\varrho_i V_i^2}{2} + \frac{B^2}{2\mu}. \qquad (13)$$

Here subscripts $_i$, $_n$, and $_e$ correspond to ions, neutrals, and electrons, respectively. The symbols $\varrho_{i,n}$ denote mass densities, $V_{i,n}$ velocities, $p_{ie,n}$ ion+electron and neutral gas pressures, B magnetic field, and $T_{i,n}$ temperatures specified by ideal gas laws,

$$p_n = \frac{k_B}{m_H\mu_n}\varrho_n T_n, \, p_{ie} = \frac{k_B}{m_H\mu_i}\varrho_i T_i. \qquad (14)$$

A gravity vector is $g = [0, -g, 0]$ with its magnitude $g = 274.78$ m s^{-2}, α_c is the coefficient of collisions between ion and neutral particles (e.g., Oliver et al. 2016; Ballester et al. 2018, and references cited therein). Q_R^i is a radiative loss term that is implemented here in the framework of Abbett & Fisher (2012) in the low atmospheric regions and of thin radiation (Moore & Fung 1972) in the top atmospheric layers, $q_{i,n}$ are thermal conduction terms (Spitzer 1962), $\mu_i = 0.58$ and $\mu_n = 1.21$ are the mean masses of respectively ions and neutrals, which are taken from the OPAL solar abundance model (e.g., Vögler et al. 2004), m_H is the hydrogen mass, k_B is the Boltzmann constant, $\gamma = 1.4$ is the specific heat ratio, and μ is magnetic permeability of the medium. The other symbols have their standard meanings.

We consider the case of the z-invariant system and start our simulations at $t = 0$ s with the hydrostatic equilibrium being supplemented by transversal and vertical magnetic fields, given

as $B = [B_x, B_y, B_z] = [0, B_0, B_0]$, where $B_0 = 5/\sqrt{2}$ Gs. The transversal component, B_z, results in Alfvén waves being linearly coupled to magnetoacoustic waves. The presence of Alfvén waves is essential in the model, because in the nonlinear regime they are capable of driving vertical flow (e.g., Hollweg 1986; Murawski 1992; Shestov et al. 2017).

In the framework of the implemented magnetic field model we set at $t = 0$ s identical hydrostatic temperature for ions and neutrals, $T_i(y) = T_n(y) = T(y)$ (Martínez-Gómez et al. 2016, 2017; Oliver et al. 2016; Soler et al. 2017; Srivastava et al. 2018). This temperature is determined by the semiempirical model of Avrett & Loeser (2008) that is extrapolated into the corona.

The hydrostatic equilibrium is restructured in time by the solar granulation. This granulation appears naturally in the convection zone, which is convectively unstable. First signs of granulation are seen already after about 5 minutes from the start of the simulations with a fully developed state occurring after about 3000 s of the solar time.

3. Numerical Simulations of Two-fluid Plasma Outflows

To solve two-fluid equations numerically, we use the JOANNA code (Wójcik et al. 2018). We set in our numerical experiments the Courant–Friedrichs–Lewy number equal to 0.9 and choose a second-order accuracy in space and a four stage, third-order strong stability preserving the Runge–Kutta method (Durran 2010) for integration in time, supplemented by adopting the Harten–Lax–van Leer Discontinuities approximate Riemann solver (Miyoshi & Kusano 2005) and the Global Lagrange Multiplier method of Dedner et al. (2002). The simulation box extends from the convection zone (2.56 Mm below the bottom of the photosphere) to the corona (up to 30 Mm above the photosphere) in the y-direction and horizontally from $x = -2.56$ Mm to $x = 2.56$ Mm. This box is divided into several patches. The bottom region, specified by -2.56 Mm $\leqslant y \leqslant 7.68$ Mm, is covered by the 1024×1024 identical cells, leading to the spatial resolution of 10 km. Within the layer of 7.68 Mm $\leqslant y \leqslant 30$ Mm, we implement several patches of progressively larger cells along the y-direction. On the left and right sides of the simulation box we set periodic boundary conditions, while the top and bottom ghost cells are filled by plasma quantities equal to their equilibrium values. The layer for the optical depth greater than 10 is additionally heated by implementing an extra source term in the energy equation of ions that balances the energy losses there.

Figure 1 (colormap) shows typical spatial profiles of $\log \varrho_i$ (top) and the vertical component of ion velocity (bottom). The granulation excites a wide range of waves deep in the photosphere. Some of these waves steepen into shocks while propagating upwards. This steepening results from wave amplitude growth with height, and chromospheric jets are excited (top). The plasma above the apices of these jets moves upwards reaching its maximum speed of around 100 km s^{-1} (bottom). The outflowing plasma essentially follows open magnetic field lines (black lines) of magnetic funnels that are formed by the granulation. The footpoints of these funnels are rooted deep in the photosphere between granules, while higher up, above the transition region, the magnetic field lines remain essentially vertical. The plasma outflows form strand-like structures along magnetic field lines in the corona, with subsiding plasma taking place at lower altitudes.
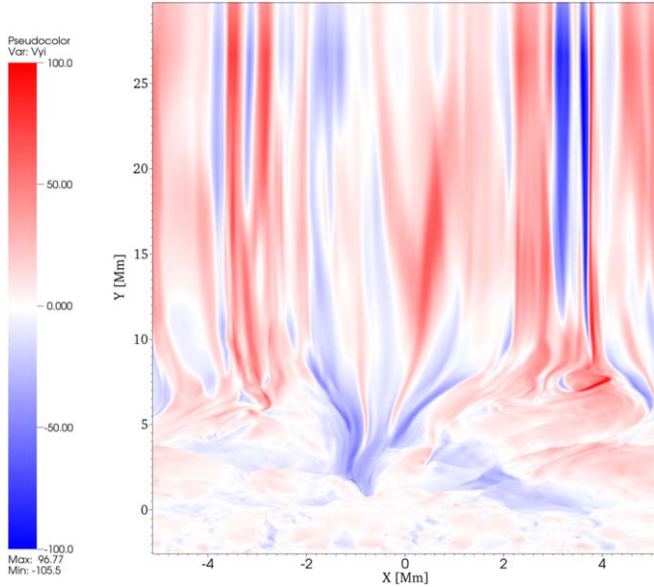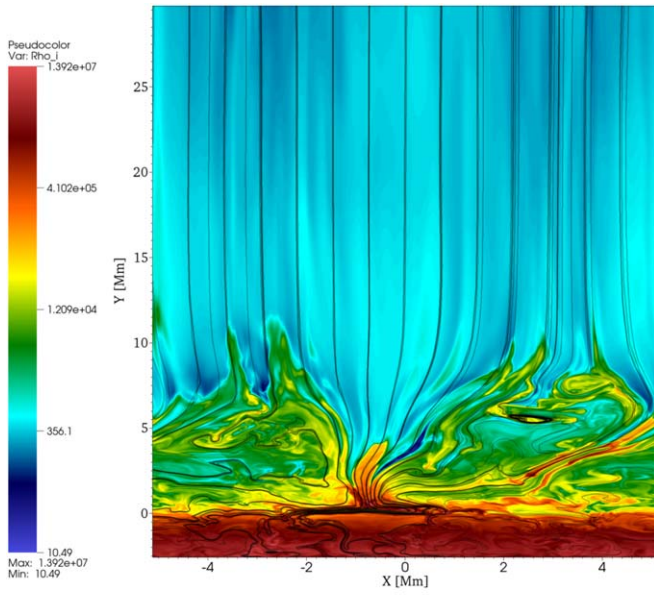
Figure 2. Spatial profile of the vertical component $V_{iy}(x, y)$, expressed in units of $1\ \mathrm{km\ s^{-1}}$ for the spatial resolution of $20\ \mathrm{km} \times 20\ \mathrm{km}$.

Figure 1. Typical spatial profiles of $\log \varrho_i$ overlayed by magnetic field (solid lines; top) and vertical component of velocity $V_{iy}(x, y)$ (bottom). Ion mass density is given in units of $10^{-18}\ \mathrm{g\ cm^{-3}}$ and V_{iy} is expressed in units of $1\ \mathrm{km\ s^{-1}}$.

We have run the code with extra nonadiabatic terms such as thermal conduction and magnetic diffusion included along with radiation. However, due to the computational effort we have not yet obtained satisfactory results. We have also run the code with the spatial resolution of $20\ \mathrm{km} \times 20\ \mathrm{km}$ and the results are shown in Figure 2. The results are close to those shown in Figure 1 (bottom), which confirms that the chosen spatial resolution of $10\ \mathrm{km} \times 10\ \mathrm{km}$ is sufficient to resolve plasma outflows.

Figure 3 displays a time–distance plot of the vertical component of ion velocity that is averaged over the whole horizontal distance, $\langle V_{iy} \rangle$. The plasma jets emerge from the chromospheric background and move into the corona. Some of the injected plasma subsides rapidly after reaching its maximum phase (e.g., Kuźma et al. 2017; Srivastava et al. 2018). This
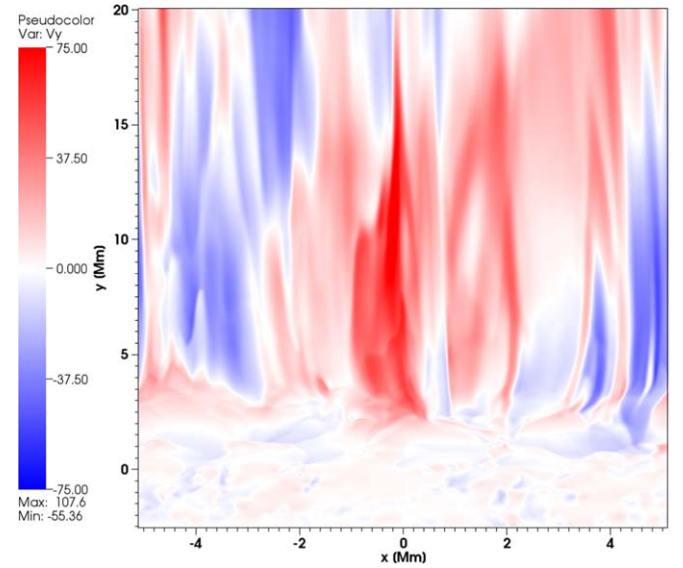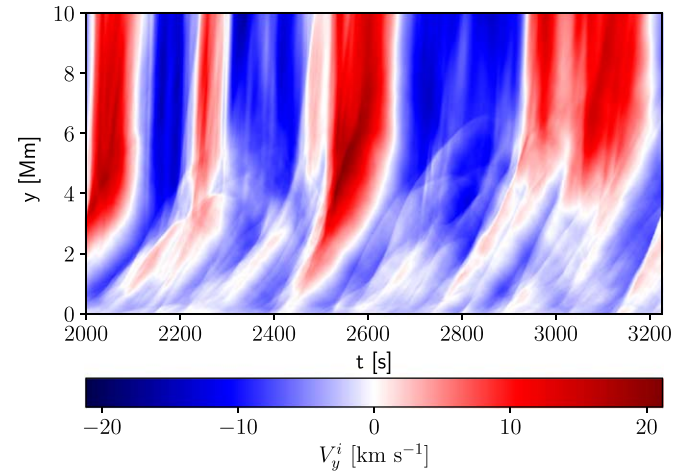

Figure 3. Time–distance plot of horizontally averaged vertical component of ion velocity, $\langle V_{iy}(y, t) \rangle$.

entire process is driven by ongoing granulation in the photosphere. Analyzing $\langle V_{iy}(y, t) \rangle$ we find that the solar corona experiences about $1-3$ minute period oscillations and $\langle V_{iy} \rangle$ reaches a magnitude of $10-20\ \mathrm{km\ s^{-1}}$ at $y = 8\ \mathrm{Mm}$ and it grows with height. The physical properties of these outflows are akin to the flow characteristics reported by Tu (2005).

Figure 4 (top) illustrates the time–distance plot of the horizontally averaged total vertical ion mass flux, $F_m(y, t) = \langle \varrho_i V_{iy} \rangle$, which attains its maximum in the photosphere and lower chromosphere and falls off with height due to rapidly decreasing ion mass density. However, even above the transition region the estimated magnitude of this mass flux lays within the range of 10^{-6} and $10^{-5}\ \mathrm{g\ cm^{-2}\ s^{-1}}$ and it matches the prediction for solar mass losses in the low corona (Withbroe & Noyes 1977).

Vertical component of ion energy flux transported through the medium can be calculated as $F_E(x, y, t) = \varrho_i V_i^2 V_{iy}/2$. The time–distance plot of horizontally averaged vertical energy flux, $\langle F_E(y, t) \rangle$, is shown in Figure 4 (bottom). We see that plasma escaping into the corona above the transition region
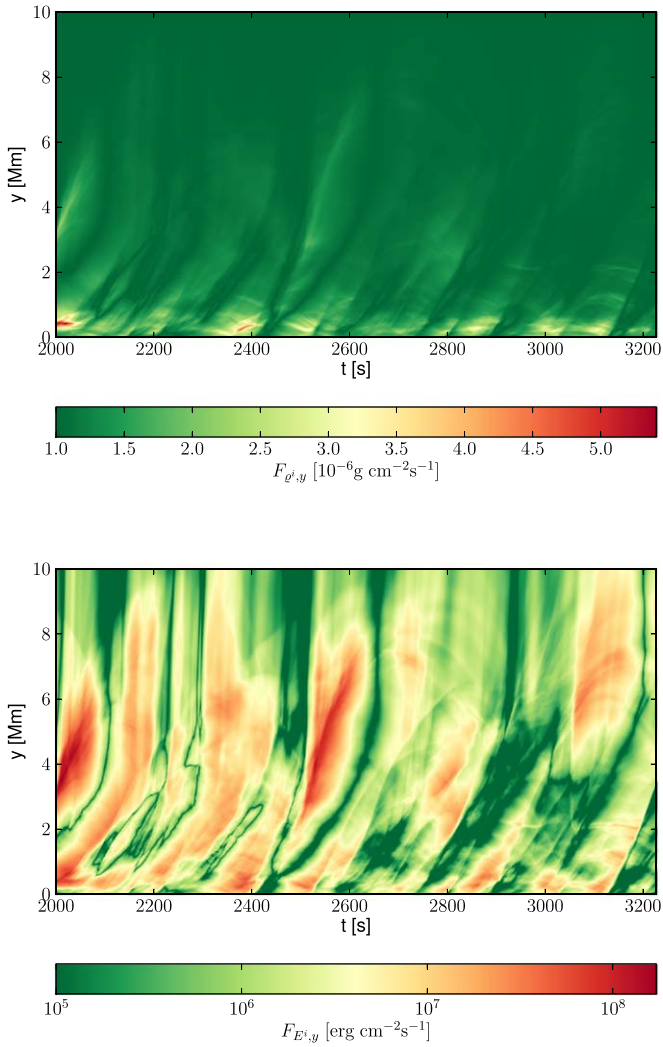
Figure 4. Time–distance plots of the horizontally averaged total vertical mass, $\langle F_m(y, t)\rangle$, (top) and energy, $\langle F_E(y, t)\rangle$, (bottom) fluxes.

Figure 5. Vertical variation of the temporarily and horizontally averaged mass, $\langle F_m(y)\rangle$ (top), and energy, $\langle F_E(y)\rangle$ (bottom), fluxes.

carries a significant amount of energy (orange and yellow patches). By comparison with time–distance plots of $\langle V_{i\,y}\rangle$ (Figure 3) we infer that the energy flux associated with the upflowing plasma is higher than for the descending plasma. Note that the obtained values lay within the range of theoretical findings for energy losses in the upper chromosphere, transition region, and low corona (Withbroe & Noyes 1977).

Figure 5 shows vertical variation of the temporarily and horizontally averaged mass, $\langle F_m\rangle$ (top), and energy, $\langle F_E(y)\rangle$ (bottom), fluxes. Note that $\langle F_E(y)\rangle$ grows abruptly within the region of $0 < y < 0.5$ Mm, where the dense photospheric plasma experiences a push from the below operating granulation. Higher up, that is, for $y > 0.5$ Mm, $\langle F_m(y)\rangle$ declines with height attaining a value of 10^{-6} g cm^{-2} s^{-1} at $y = 10$ Mm. On the other hand, $\langle F_E(y)\rangle$ remains close to 10^7 erg cm^{-2} s^{-1} in the entire chromosphere and transition region, attaining its local maxima at $y = 0.25$ Mm and $y = 3.5$ Mm. Higher up, it slowly falls off with height, reaching its value of $5 \cdot 10^5$ erg cm^{-2} s^{-1} at $y = 10$ Mm.

4. Discussion and Summary

Within the framework of two-fluid equations for ion-neutral plasma, we performed numerical simulations of the origin of

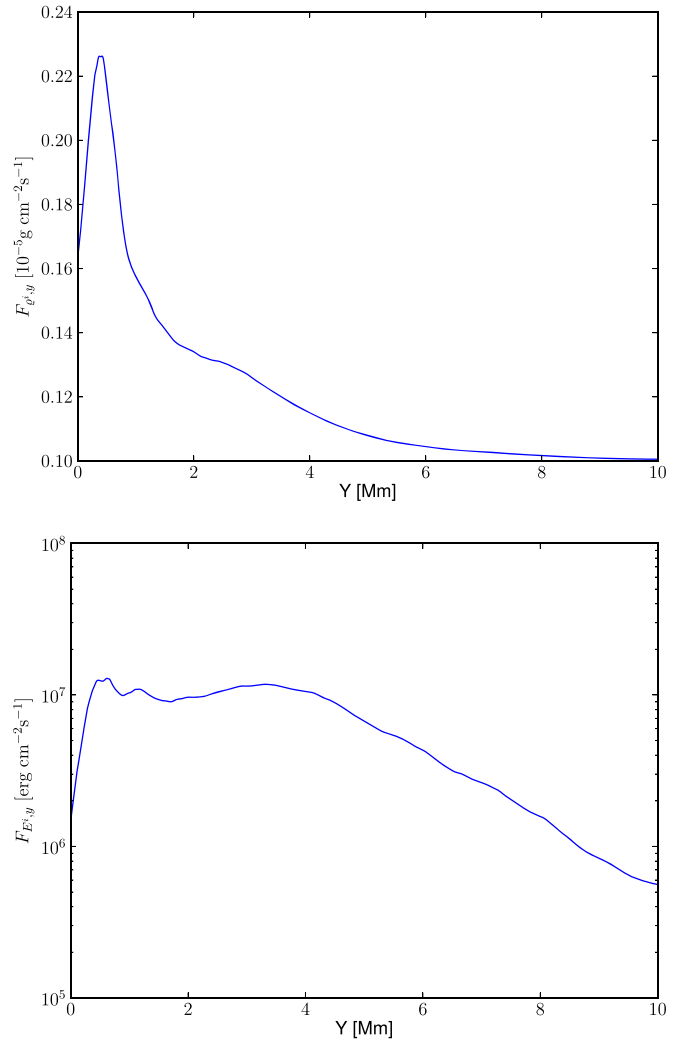the solar wind that results from plasma outflows. These outflows are associated with jets excited by the solar granulation, which develops in the medium with a initially straight magnetic field overlaying a hydrostatic equilibrium. This configuration well mimics the expanding open magnetic field region in a polar coronal hole. Our simulations show that this configuration is restructured later on by granulation, which operates in the photosphere. The whole scenario is associated with the energy and mass leakage into higher atmospheric layers in the form of plasma outflows. Our results successfully match the expected values of mass and energy losses in the upper chromosphere, transition region, and low corona (Withbroe & Noyes 1977).

It is noteworthy here that Tu (2005) obtained a correlation of the Doppler-velocity and radiance maps of spectral lines emitted by various ions (Ne VIII, C IV, and Si II) with the force-free magnetic field that was extrapolated from the photospheric magnetogram (*SOHO*/MDI) in a polar coronal hole. Tu found that Ne VIII ions mostly radiate around the height of 20 Mm above the photosphere, where they reveal the outflow speed of about 10 km s^{-1}, while C IV ions with no average flow speed form essentially around the altitude of 5 Mm. Hence, Tu inferred that the plasma outflows start in the coronal funnels at altitudes in between 5 and 20 Mm. Yang et al. (2013) proposed

that magnetic reconnection, which took place in the open and closed magnetic field region, triggers the plasma outflows observed by Tu (2005). The results of our simulations performed with a novel two-fluid model of a partially ionized solar atmospheric plasma confirm these observational findings.

Ten years before the plasma outflows were announced by Tu (2005), there was essentially no report on finely structured jets. The exceptions were spicules/macrospicules diversely filling the chromosphere and contributing to the mass cycle of the corona (e.g., Wedemeyer-Böhm et al. 2012; Tian et al. 2014). In the limit of current observational resolution, it is established that the overlaying plasma outflows in the corona must have originated due to the contribution from various plasma ejecta. Therefore, without emphasizing a particular type of a jet, we simulated the solar granulation that resulted in jets and studied their contribution to formation of the solar wind.

In summary, we investigated formation of plasma outflows between 5 and 10 Mm above the photosphere in the open magnetic field region in a coronal hole as observed by Tu (2005). The outflows in such regions consist of continuous streaming of plasma particles from the lower solar atmosphere outward. We point out its linkage to the granulation and associated with them the ubiquitous chromospheric jets that lead to mass and energy leakage into the inner corona. Our model is based on gravitationally stratified and partially ionized bottom layers of the solar atmosphere with adequate temperature and magnetic field conditions to mimic the ion-neutral plasma outflows. Our studies determine that multiple jets excited by operating in the photosphere granulation are able to stimulate continuous plasma outflows in the solar atmosphere, which may result in the fast solar wind at higher altitudes in the solar corona.

ORCID iDs

D. Wójcik ⓘ https://orcid.org/0000-0002-4200-3432

References

Abbett, W. P., & Fisher, G. H. 2012, SoPh, 277, 3
Arber, T. D., Brady, C. S., & Shelyag, S. 2016, ApJ, 817, 94
Avrett, E., & Loeser, R. 2008, ApJS, 175, 229
Ballester, J. L., Alexeev, I., Collados, M., et al. 2018, SSRv, 214, 58
Bierman, L. 1951, ZA, 29, 274
Chmielewski, P., Murawski, K., Musielak, Z. E., & Srivastava, A. K. 2014, ApJ, 793, 43
De Pontieu, B., McIntosh, S. W., Carlsson, M., et al. 2007, Sci, 318, 1574
Dedner, A., Kemm, F., Kröner, D., et al. 2002, JCoPh, 175, 645
Durran, D. R. 2010, Numerical Methods for Fluid Dynamics (Berlin: Springer)
Goossens, M., Andries, J., Soler, R., et al. 2012, ApJ, 753, 111
He, J.-S., Tu, C.-Y., & Marsch, E. 2008, SoPh, 250, 147
Hollweg, J. V. 1978, SoPh, 56, 305
Hollweg, J. V. 1981, SoPh, 70, 25
Hollweg, J. V. 1986, ApJ, 306, 730
Hollweg, J. V., Jackson, S., & Galloway, D. 1982, SoPh, 75, 35
Kayshap, P., Banerjee, D., & Srivastava, A. K. 2015, SoPh, 290, 2889
Kayshap, P., Srivastava, A. K., Murawski, K., & Tripathi, D. 2013, ApJL, 770, L3
Krieger, A. S., Timothy, A. F., & Roelof, E. C. 1973, SoPh, 29, 505
Kudoh, T., & Shibata, K. 1999, ApJ, 514, 493
Kuźma, B., Murawski, K., Kayshap, P., et al. 2017, ApJ, 849, 78
Marsch, E. 2006, LRSP, 3, 1
Marsch, E., Tian, H., Sun, J., Curdt, W., & Wiegelmann, T. 2008, ApJ, 685, 1262
Martínez-Gómez, D., Soler, R., & Terradas, J. 2016, ApJ, 832, 101
Martínez-Gómez, D., Soler, R., & Terradas, J. 2017, ApJ, 837, 80
Martínez-Sykora, J., Pontieu, B. D., Hansteen, V. H., et al. 2017, Sci, 356, 1269
Matsumoto, T., & Suzuki, T. K. 2012, ApJ, 749, 8
McIntosh, S. W. 2012, SSRv, 172, 69
McIntosh, S. W., De Pontieu, B., & Mats, C. 2011, Natur, 475, 477
Miyoshi, T., & Kusano, K. 2005, JCoPh, 208, 315
Moore, R. L., & Fung, P. C. W. 1972, SoPh, 23, 78
Murawski, K. 1992, SoPh, 139, 279
Nakariakov, V. M., Roberts, B., & Murawski, K. 1997, SoPh, 175, 93
Ofman, L. 2005, SSRv, 120, 67
Ofman, L., Davila, J. M., & Steinolfson, R. S. 1995, ApJ, 444, 471
Oliver, R., Soler, R., Terradas, J., & Zaqarashvili, T. V. 2016, ApJ, 818, 128
Parker, E. N. 1965, SSRv, 4, 666
Shestov, S. V., Nakariakov, V. M., Ulyanov, A. S., Reva, A. A., & Kuzin, S. V. 2017, ApJ, 840, 64
Soler, R., Terradas, J., Oliver, R., & Ballester, J. L. 2017, ApJ, 840, 20
Spitzer, L. 1962, Physics of Fully Ionized Gases (New York: Interscience)
Srivastava, A. K., & Dwivedi, B. N. 2006, JApA, 27, 353
Srivastava, A. K., Murawski, K., Kuźma, B., et al. 2018, NatAs, 2, 951
Srivastava, A. K., Shetye, J., & Murawski, K. 2017, NatSR, 7, 43147
Sterling, A. C. 2000, SoPh, 196, 79
Suzuki, T. K., & Inutsuka, S. 2005, ApJL, 632, L49
Tian, H., Li, G., Reeves, K. K., et al. 2014, ApJL, 797, L14
Tian, H., Marsch, E., Curdt, W., & He, J. 2009, ApJ, 704, 883
Tian, H., Tu, C., Marsch, E., He, J., & Kamio, S. 2010, ApJL, 709, L88
Tu, C.-Y. 1987, SoPh, 109, 149
Tu, C.-Y. 2005, Sci, 308, 519
Vögler, A., Shelyag, S., Schüssler, M., et al. 2004, A&A, 429, 335
Wedemeyer-Böhm, S., Scullion, E., Steiner, O., et al. 2012, Natur, 486, 505
Withbroe, G. L., & Noyes, R. W. 1977, ARA&A, 15, 363
Wójcik, D., Murawski, K., & Musielak, Z. E. 2018, MNRAS, 481, 262
Yang, L., He, J., Peter, H., et al. 2013, ApJ, 777, 16
Yang, L., Lee, L. C., Chao, J. K., et al. 2016, ApJ, 817, 178
Zaqarashvili, T. V., & Erdélyi, R. 2009, SSRv, 149, 355
Zaqarashvili, T. V., & Roberts, B. 2006, A&A, 452, 1053
Zirker, J. B. 1977, RvGeo, 15, 257